


# COMPARATIVE ANALYSIS OF DIFFERENT NUMERICAL SIMULATION METHODS FOR PROPELLER SLIPSTREAM

Jiawen He[1,2*], Yue Zhao[1,2], Xinyuan Wei[1,2], Tieren Chen[1,2], Yong Yang[1,2]

[1]School of Aeronautics, Northwestern Polytechnical University, Xi'an, 710072, PR China
[2]National Key Laboratory of Aircraft Configuration Design, Xi'an, 710072, PR China

## Abstract

Propeller powered aircraft still plays an important role in both civil and military aviation, and propeller slipstream has a large impact on downstream aircraft components[2]. Full rotating propeller with dynamic slid-patching method[2] is one of traditional slipstream simulation methods, here after, this method is defined as full blade method(FBM). However, due to the difficulty of overall grid generation ,especially for structured grid, this paper employs an unsteady method, replacing the real rotating propeller with loads of pressure and swirl velocity jump restricted in the region swept by the real propeller blade, here after, this method is defined as actuator blade method(ABM). The pressure and swirl velocity jump can be transferred from the simulation of real rotating propeller. As there is no need for the consideration of the real propeller for whole aircraft grid generation, ABM can reduce the workload of grid generation.

In order to investigate the differences between two methods, slipstream details of single propeller and the intensity of pressure exerted by the propeller slipstream on the wing will be revealed. In this paper, two geometry configurations are employed, including a single propeller with a simplified nacelle and a propeller-wing integrated configuration. Specific work in this article includes:

(1) Three methods are employed for numerical simulations of single propeller slipstream, including full mesh rotation method using point-to-point grid, dynamic slid-patching method using dynamic patched grid and ABM using point-to-point grid. The detailed flow field properties in the slip-stream are investigated to show the consistence between ABM and real propeller.

(2) Under the same computational conditions, the influences of different parameter settings on the numerical resolution of the wake vortex obtained by ABM are analyzed. The unsteady simulation parameters, including non-dimensional time step (DT), number of inner-iterations (NCYC) and so on, are adjusted to analyze the effects of different parameter settings on the numerical resolution of the wake vortex.

(3) Additionally, numerical simulations of the propeller-wing configuration are carried out using the FBM and ABM separately, comparative analysis is performed on the pressure fluctuation due to the unsteady propeller slip stream on the wing surface.

**Keywords:** Propeller Slipstream, Unsteady Numerical Simulation, Full-Blade-Method(FBM), Actuator Blade Method(ABM)

## 1. General Introduction

The influence of the propeller on the aircraft is mainly concerned in the effect of the propeller slipstream on the wing and other control surface. To gain a deeper understanding of the aerodynamic interference of aircraft components affected by propeller slip stream, aircraft designers have initiated theoretical and experimental investigations since the 1930s[3]. Full blade method (FBM) and actuator disk method (ADM)[1][4][10] are the most common numerical methods for studying the propeller slipstream effects. The former involves numerical simulation of the unsteady flow field associated

with propeller rotation, which can capture unsteady flow phenomena such as tip vortices[2]. However, the difficulty of grid generation and the huge simulation cost are inevitable; The latter is based on momentum theory[11], replacing the propeller effect with time-averaged loads distributed on the actuator disk[5]. The simplified geometric model significantly reduces the difficulty of grid generation, furthermore, the steady flow simulation drastically reduces computational time[6].

Although ADM makes fast slipstream simulation possible, but it cannot reflect unsteady fluctuations because only time-averaged loads are implemented the governing equations[8].

To reflect the unsteady characteristics of propeller slipstream, actuator blade method is developed. In this model, momentum source terms are imposed at positions of actual blade transient locations.

In this paper, three strategies are employed for single propeller slipstream simulation. By comparing the attenuation of vorticity and velocity at the same positions before and after the dynamic sliding interface, the diffusion across the patching interface is investigated. Based on the ABM, the impact of comparing different combinations of simulation parameters on the resolution of the simulation of propeller slipstream is investigated. At last, ABM and FBM are employed for simulating propeller-wing configuration, the unsteady oscillatory behavior of the aerodynamic coefficient and the pressure distribution on the wing surface are studied.

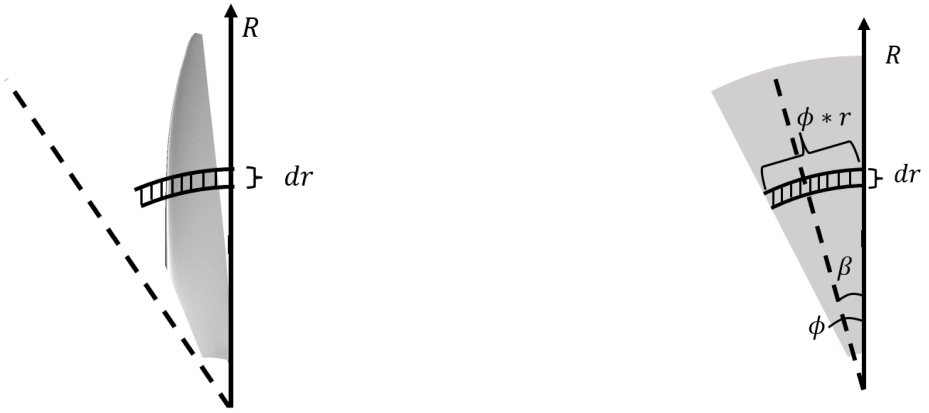
## 2. Numerical Simulation Model and Simulation method

### 2.1 ABM Modeling

ABM replaces influences induced by rotating propeller (Figure 1 (a)) with loads imposed on fan-shape-areas (Figure 1 (b)). The loads described with fan angle $\phi$ and radius of the propeller $R$ are extracted from single rotating propeller results simulated with URANS. $\theta$ is used to describe the circumferential position of the blade.

Shown in equation (1), N is number of blades and $r$ is the distance to rotation center while $\beta$ represents the angular position inside the fan-shape area. The pressure jump $\Delta p(r,\theta)$ and swirl velocity jump $\Delta V_\theta(r,\theta)$ are extracted from full blade result at radical position r and circumferential position $\theta$.The pressure and swirl jump from rotating propeller should be redistributed along the chord as $\Delta p'(r,\beta,\theta)$ and $\Delta V_\theta'(r,\beta,\theta)$. The load function $C(\xi)$ is introduced to redistribute $\Delta p(r,\theta)$ and $\Delta V_\theta(r,\theta)$ on the fan-shape-area and x represents the ratio of angular position $\beta$ to fan angle $\phi$. $C(\xi)$ ought to be smooth and derivable in the domain of definition $\xi \in [0,1]$ ,where the function should satisfy $C(0)=C(1)=0$ , $C(\xi)\geq 0$ and $\int_0^1 C(\xi)d\xi = 1$.

$$\begin{aligned}
\Delta p'(r,\beta,\theta) &= C(\xi)\frac{\Delta p(r,\theta)\bullet 2\pi}{N\bullet\phi} \\
\Delta V_\theta'(r,\beta,\theta) &= C(\xi)\frac{\Delta V_\theta(r,\theta)\bullet 2\pi}{N\bullet\phi} \\
\xi &= \frac{\beta}{\phi}\in[0,1]; r_{\min}\leq r\leq R, 0\leq\theta\leq 2\pi, 0\leq\beta\leq\phi
\end{aligned} \tag{1}$$




(a) front view of a propeller blade (b) modeling of an actuator blade

Figure 1 blade modeling

Now the load function $C(\xi)$ should be determined. First introduced by Kulfan, the class/shape transformation (CST) is a universal method to describe the distribution of analytical smooth shapes using a class function and a shape function[12]. The class function represents 2-D distribution or other smooth curves while the shape function is used to control 3-D features possessing an inherent strong smoothing capability like a wing. As there is no shock wave on real propeller blades, the loads for ABM can be described using a class function of the CST method (shown in equation (2)). A loss function $loss(N_1, N_2)$ is established in equation (3) to determine constant k, $N_1$ and $N_2$ in $C(\xi)$, where $p_i$ is the discrepancy of pressure on normalized propeller airfoils (unit chord length of 1) between upper and lower surface. $N_1$ and $N_2$ is obtained when the function $loss(N_1, N_2)$ reaches its minimum value. Then, constant k is determined in equation (4).

$$C(x) = k\xi^{N_1} \bullet (1-\xi)^{N_2}, \xi \in [0,1] \tag{2}$$

$$loss(N_1, N_2) = \sum_{i=1}^{n} \frac{(C(\xi_i) - p_i)^2}{n} \tag{3}$$

$$k = \frac{1}{\int_0^1 \xi^{N_1} \cdot (1-\xi)^{N_2} d\xi} \tag{4}$$

## 2.2 Geometry of Single Propeller with a Simplified Nacelle

The single propeller geometry is a four-meter-diameter, six-blade propeller with a simplified nacelle which is shown as Figure 2. The disk shown in Figure 3 is a special boundary to impose shifting loads corresponding to the rotating blades. The geometry information and operation conditions are given in Table 1. $Ma_\infty$ represents free stream Mach number, $n_s$ represents rotation speed ($r/s$), $T_\infty$ is temperature ($K$) and $J$ is advance ratio (defined in equation (5)). $V_\infty$ is free stream velocity ($m/s$), $n_s$ represents rotation speed of propeller ($r/s$) and $D$ represents diameter of propeller (m). A dynamic patched grid method is applied for slid-patching method while full mesh rotation method and ABM use a point-to-point grid method. The grid information is listed in Table 2.

$$J = \frac{V_\infty}{n_s D} \tag{5}$$

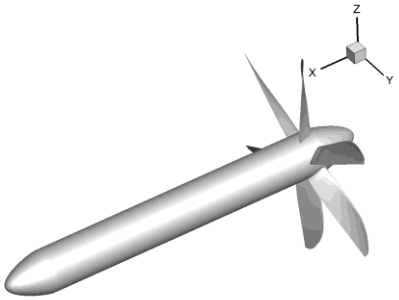


Figure 2 Geometry of single propeller for FBM

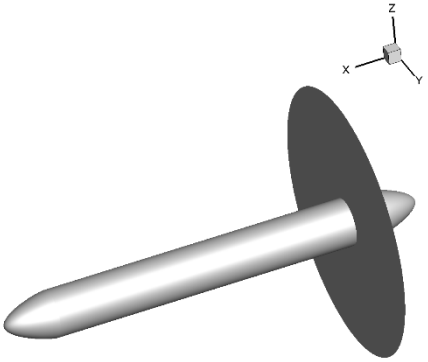


Figure 3 Geometry of single propeller for ABM

Table 1 Geometry Information and Operation Conditions of Propeller

| Parameter | $Ma_\infty$ | diameter, m | $T_\infty, K$ | $n_s, r/s$ | Reynolds number | $J$ | $\alpha$, deg |
|---|---|---|---|---|---|---|---|
| Value | 0.211 | 4 | 288.15 | 17.95 | $4.91\times10^6$ | 1.0 | 0 |

Table 2 Grid Information

| Grid Strategy | Cell Numbers |
|---|---|
| Dynamic Patched(dynamic slid-patching method) | $1.65\times10^7$ |
| Point to Point(full mesh rotation method) | $1.60\times10^7$ |
| Point to Point(ABM) | $1.62\times10^7$ |

## 2.3 Geometry of Propeller-wing Integrated Configuration

Figure 4 gives the sketch of propeller-wing configuration, in which, a propeller is mounted at the leading edge of a rectangular straight wing. The wing and the propeller are connected by a spindle-shape short nacelle. The airfoil of the wing is chosen as NACA0012 with a zero-degree installation angle. The wing has a span of 7.5m and a chord length of 2m. The rotational axis of the propeller coincides with the chord line at the wing symmetry plane. Figure 5 shows the same configuration with the rotating propeller replaced by a virtual disk, which is used in ABM simulation. The virtual disk is shown as the blue area which imposes shifting loadings. Table 3 shows the grid information of the two configurations. It can be observed that with the same grid distribution along the x-axis(the wing chordwise direction), the number of generated grids for the actuator blade-wing configurations is only half of that for the propeller-wing configuration, which significantly reduces the human power in grid generation.

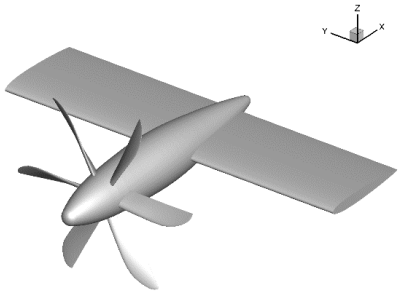


Figure 4 Propeller-Wing Configuration

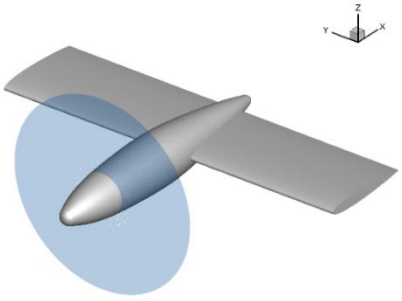


Figure 5 actuator blade-wing configuration

Table 3 Grid Information of Two Configurations

| Geometry Configuration | Cell Numbers |
|---|---|
| Propeller-wing (Dynamic Sliding Patch Mesh) | $1.55\times10^7$ |
| Actuator blade-wing (Point to Point Mesh) | $0.8\times10^7$ |

## 3. Load Transplant from Real Blade to Actuator Blade

Since the actuator blade method extracts the loads of a real propeller under operation conditions, and transplant the extracted loads to the fan-shaped shifting region. Figure 6 and Figure 7 present the pressure contour and swirl velocity momentum contour at 0.1m downstream of the actuator blade surface, respectively.

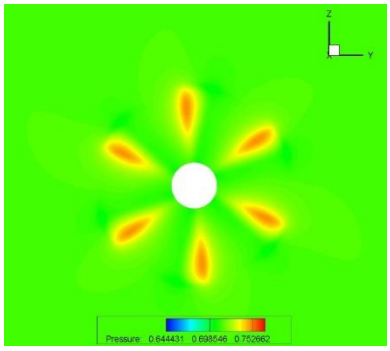


Figure 6 contour of the axial pressure of ABM

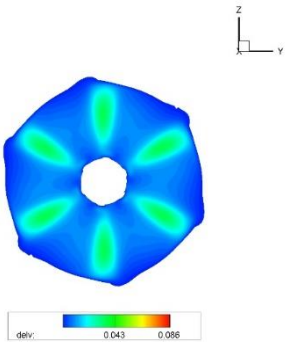
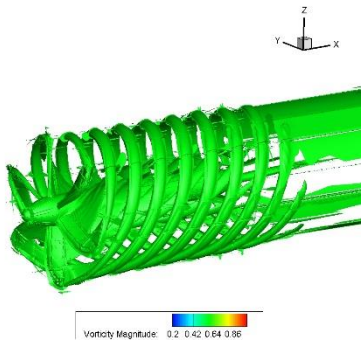


Figure 7 contour of the swirl velocity momentum of ABM

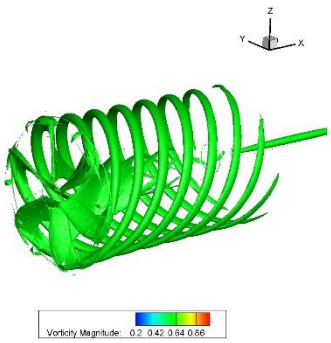
## 4. Comparison of Simulation Results for The Single Propeller Configuration

In this section, three methods are employed to perform numerical simulations of the single propeller configuration: the full mesh rotation method, the dynamic slid-patching method and the actuator blade method. Among them, the full mesh rotation method and the actuator blade method use point-to-point grids, while the dynamic slid-patching method uses a patched interface to communicate the flow information. When using a dynamic patched interface, there will be more diffusion effects due to the grid stretching and non-uniform distribution across the patching interface.

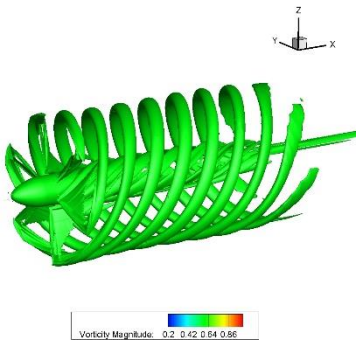
All three methods are unsteady numerical simulation approaches, using identical simulation parameters and operating conditions throughout the simulations. The results, includes vorticity, swirl velocity, and axial velocity, from the three methods are compared and analyzed. Figure 8 presents the iso-surface contours of the propeller slipstream vorticity obtained using the full mesh rotation method, the dynamic slid-patching method, and the actuator blade method, as well as the vorticity contours of the trailing vortices on the cross-section along the propeller axis.



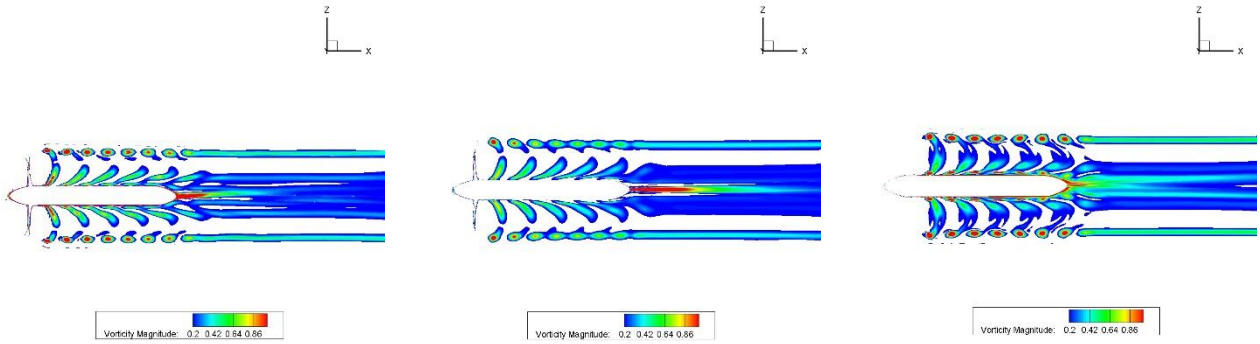
(a) iso-surface contours of full mesh rotation method



(b) iso-surface contours of dynamic slid patching method



(c) iso-surface contours using actuator blade method




(d) vorticity contours using full mesh rotation method

(e) vorticity contours of dynamic slid-patching method

(f) vorticity contours using actuator blade method

Figure 8 Iso-surface Contours and Vorticity Contours Using Three Methods

From the iso-surface contours of the vortex vorticity, it can be seen that under the same computational conditions, the strength of downstream vortex simulated by the dynamic slid-patching method is weaker compared to the other two methods. In contrast, the tip vortex strength obtained by the full mesh rotation method and the actuator blade method is well-preserved. From the vorticity contours on the propeller axis cross-section, it is observed that the tip vortex intensity simulated by the dynamic slid-patching method is more diffused, and is less concentrated.

Based on the qualitative conclusions obtained from the three methods, a detailed quantitative analysis is conducted. For the dynamic slid-patching method, the dynamic sliding interface in the geometric configuration is located at the axial position x=4.42125. To investigate the changes in velocity components and vorticity magnitude across the interface, six cross-sections are selected upstream and downstream of the interface. Integrations of the swirl velocity, axial velocity and vorticity are performed on these cross-sections to compare the changes across the interface. The results from the three methods are compared in Table 4,7 and 8 at each cross-section respectively.

From Table 4-8, it can be seen that the change in vorticity simulated by the dynamic slid-patching method decreases from 3.629 to 2.946 across the patch interface, a reduction approximately 20%. In contrast, the full mesh rotation method and the actuator blade method show reductions of only 0.012 and 0.002. For the swirl velocity, the change obtained by the dynamic slid-patching method decreases from 0.5746 to 0.5706, while the full mesh rotation and the actuator blade methods decrease by 0.0013 and 0.0001, respectively. Clearly, the diffusion in the dynamic slid-patching method is significantly larger.

In summary, although the tables show the integral results, it can be seen that the propeller slipstream simulated by the dynamic slid-patching method suffers more diffusion across the dynamic sliding interface.

Table 4 Integral Values of Vorticity Using Three Different Methods

| Axial Location/m | 4.419 | 4.420 | 4.421 | 4.422 | 4.423 | 4.424 |
|---|---|---|---|---|---|---|
| Dynamic Slid-patching Method | 3.684 | 3.653 | 3.629 | 2.946 | 2.940 | 2.935 |
| Full Mesh Rotation Method | 4.343 | 4.330 | 4.324 | 4.312 | 4.288 | 4.271 |
| Actuator Blade Method | 3.441 | 3.440 | 3.439 | 3.437 | 3.436 | 3.434 |

Table 5 Integral Values of swirl Velocity Using Three Different Methods

| Axial Location/m | 4.419 | 4.420 | 4.421 | 4.422 | 4.423 | 4.424 |
|---|---|---|---|---|---|---|
| Dynamic Slid-patching Method | 0.5736 | 0.5742 | 0.5746 | 0.5706 | 0.5711 | 0.5720 |
| Full Mesh Rotation Method | 0.5846 | 0.5841 | 0.5853 | 0.5840 | 0.5844 | 0.5846 |
| Actuator Blade Method | 0.5634 | 0.5633 | 0.5633 | 0.5632 | 0.5631 | 0.5631 |

Table 6 Integral Values of Axial Velocity Using Three Different Methods

| Axial Location/m | 4.419 | 4.420 | 4.421 | 4.422 | 4.423 | 4.424 |
|---|---|---|---|---|---|---|
| Dynamic Slid-patching Method | 15.055 | 15.057 | 15.059 | 14.898 | 14.899 | 14.900 |
| Full Mesh Rotation Method | 15.065 | 15.066 | 15.068 | 15.069 | 15.071 | 15.072 |
| Actuator Blade Method | 14.987 | 14.989 | 14.991 | 14.993 | 14.994 | 14.996 |

After analyze the significant changes caused by the dynamic slid-patching method in numerical simulations, the distributions of axial velocity and swirl velocity at different axial positions downstream of the propeller are further examined. Cross-sections are selected at intervals of 0.5R along the axis downstream of the propeller, with four axial positions selected: 0.5R,1.0R,1.5R and 2.0R. At these four cross-sections, the radial distributions of the axial velocity and swirl velocity are analyzed. Figure 9 gives the locations of the cross-section perpendicular to the axial direction, while Figure 10-11 show the corresponding axial and swirl velocity profiles at these locations. In Figure 10 and Figure 11, FBM_p-p represents the full mesh rotation method, FBM_dyp represents the dynamic slid-patching method and ABM represents the actuator blade method.

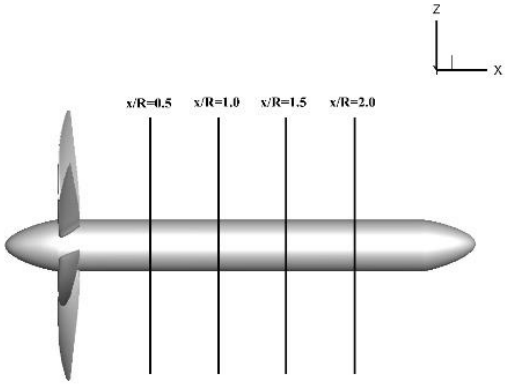
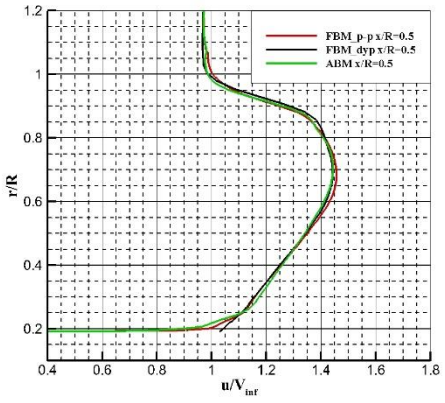
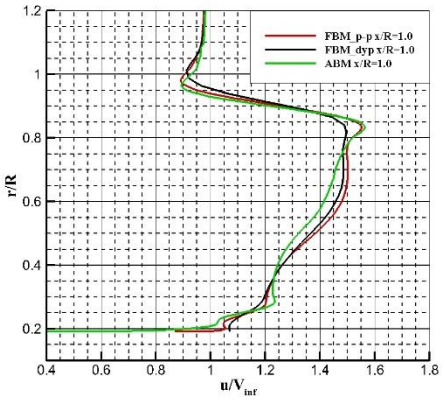



Figure 9 Schematic Sketch of Different Axial Cross-section Positions

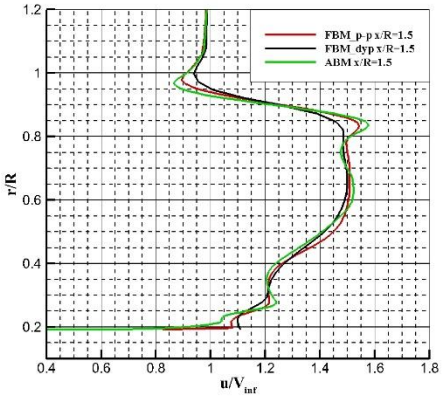
From Figure 10, it can be seen that at the axial position x=0.5R, the propeller slipstream is barely affected by the dissipation at the sliding interface, and the axial velocity profiles obtained by the three methods are in good agreement. At x=1.0R, under the combined influence of the sliding interface dissipation and the natural dissipation of the slipstream, the peak value of the distribution curve simulated by the dynamic slid-patching method is lower, while the results of the other two methods remain in good agreement. At x=1.5R and 2.0R, the results of actuator blade method exhibit the highest peak values. The overall trend of these curves shows a good agreement.

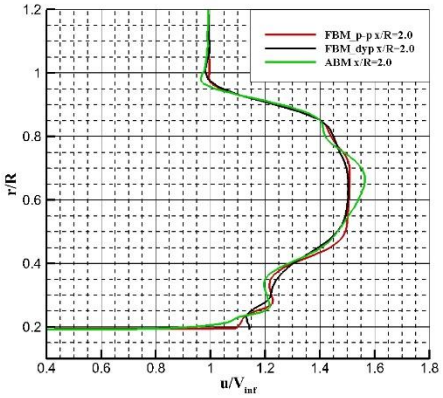



(a) axial position at x=0.5R




(b) axial position at x=1.0R

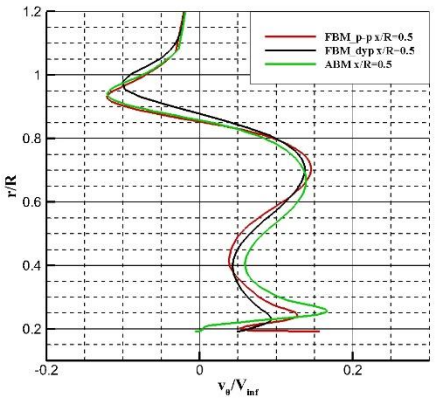


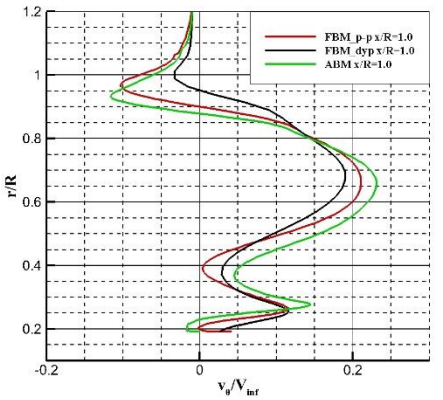




(c) axial position at x=1.5R (d) axial position at x=2.0R

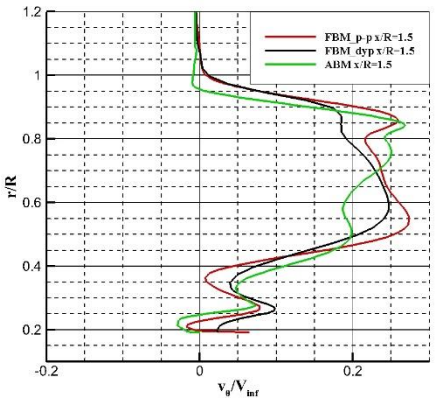
Figure 10 Dimensionless Axial Velocity Distribution at Different Axial Positions

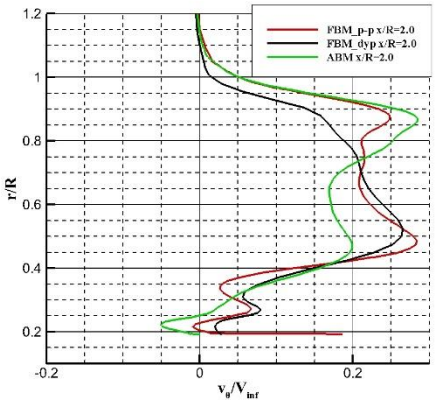
From Figure 11, it can be seen that at the axial position x=0.5R, the swirl velocity profiles obtained by the three methods are in good agreement where r/R ranges from 0.6 to 1.0. At the axial position x=1.0R,1.5R and 2.0R, due to the numerical dissipation and dispersion, the swirl velocity distributions obtained by the three methods are not in a good agreement but the general developed trends are identical.




(a) axial position at x=0.5R (b) axial position at x=1.0R




(c) axial position at x=1.5R (d) axial position at x=2.0R

Figure 11 Dimensionless swirl Velocity Distribution at Different Axial Positions

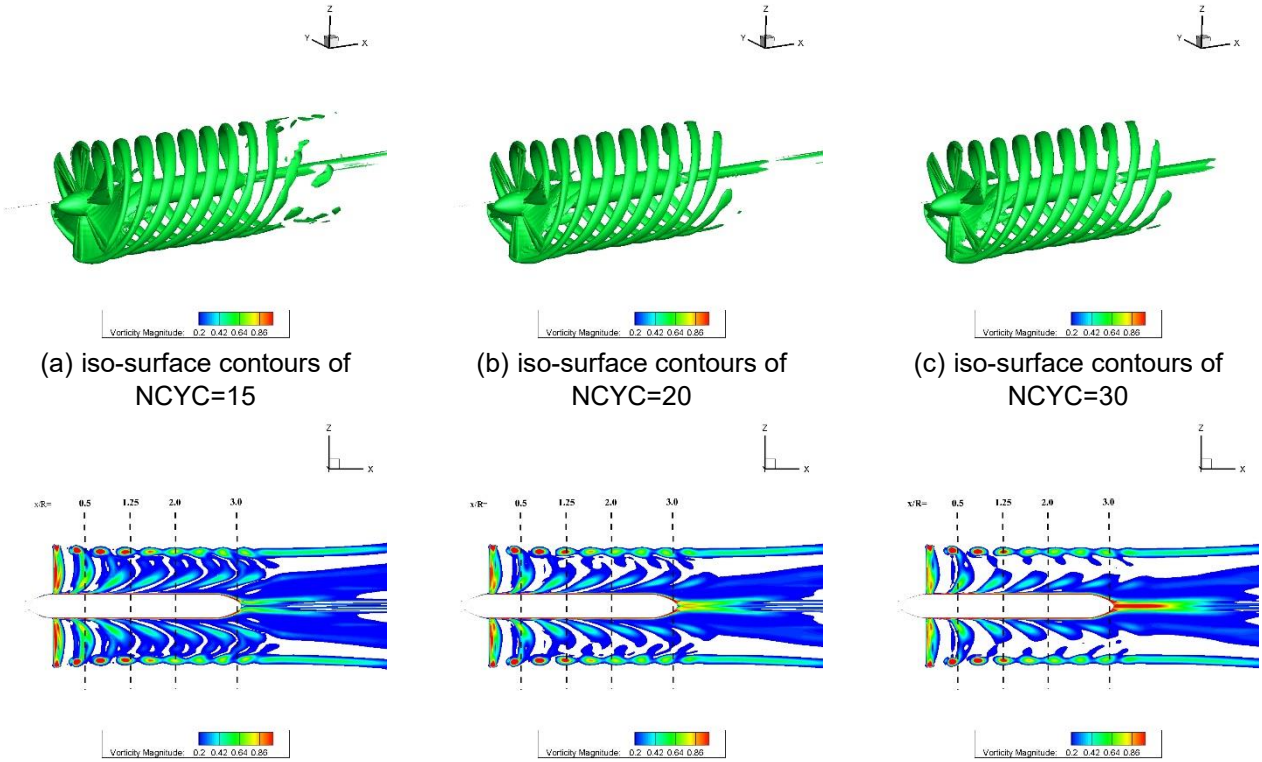
## 5. Effects of Different Simulation Parameters on the Dynamic Blade Method

To investigate the influence of different simulation parameter settings on the resolution of downstream vorticity simulated by the actuator blade method, this section gives a systematic survey for the effects of simulation parameters. These parameters include the unsteady time step (DT), the inner iteration CFL number (CFLTAU), and the number of inner iterations (NCYC).

### 5.1 Influence of NCYC

This section analyzes the effect of NCYC while keeping other simulation parameters constant. DT is set to 0.08, CFLTAU is set to 1.0, and NCYC takes values of 15, 20 and 30, respectively.

Figure 12 presents the iso-surface contours of the propeller slipstream vorticity and the vorticity contours on the axial cross-section under different NCYC settings. It can be observed from Figure 12 that, with other parameters unchanged, as NCYC increases, the iterations within each unsteady time step become more sufficient. Consequently, the vortex morphology becomes gradually clearly, and the adhesion between the blade tip vortex and the blade root vortex disappears.




(a) iso-surface contours of NCYC=15 (b) iso-surface contours of NCYC=20 (c) iso-surface contours of NCYC=30

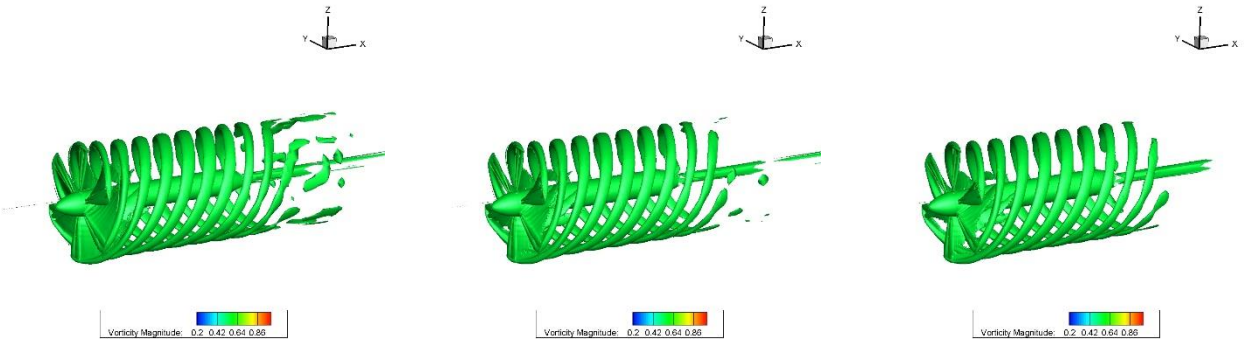
(d) vorticity contours of NCYC=15 (e) vorticity contours of NCYC=20 (f) vorticity contours of NCYC=30

Figure 12 The Influence of Different NCYC Settings on the Propeller Slipstream

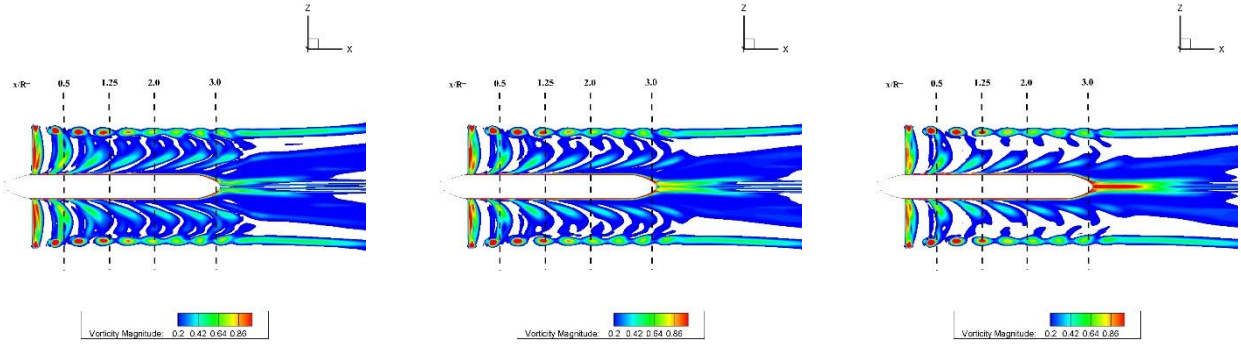
### 5.2 Influence of CFLTAU

This section analyzes the effect of CFLTAU while keeping other simulation parameters constant. DT is set to 0.08, NCYC is set to 10, and CFLTAU takes values of 1.5, 2.0, and 3.0, respectively.

Figure 13 presents the iso-surface contours of the propeller wake vorticity and the vorticity contours on the axial cross-section under different CFLTAU settings. It can be observed from Figure 13 that, with other parameters unchanged, as CFLTAU increases, the iterations within each unsteady time step become more sufficient. Consequently, the vortex morphology gradually becomes clearer, and the adhesion between the blade tip vortex and the blade root vortex disappears.




(a) iso-surface contours of CFLTAU=1.5 (b) iso-surface contours of CFLTAU=2.0 (c) iso-surface contours of CFLTAU=3.0



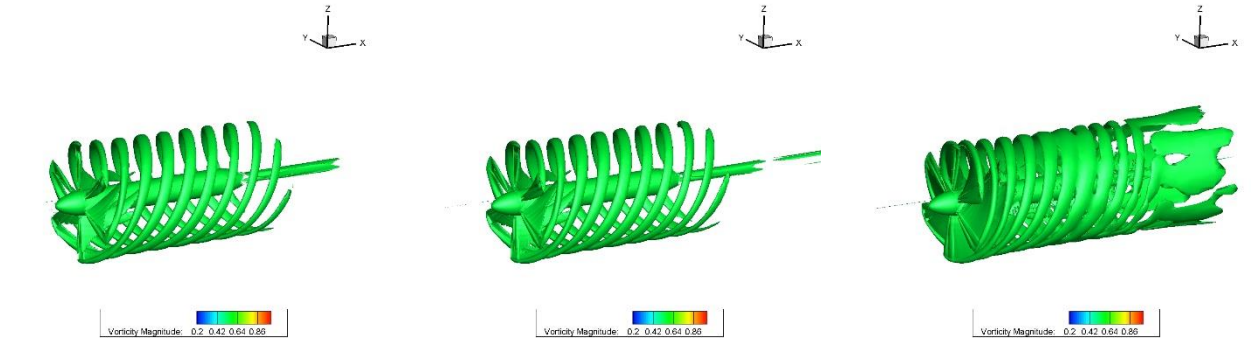

(d) vorticity contours of CFLTAU=1.5 (e) vorticity contours of CFLTAU=2.0 (f) vorticity contours of CFLTAU=3.0

Figure 13 The Influence of Different CFLTAU Settings on the Propeller Slipstream

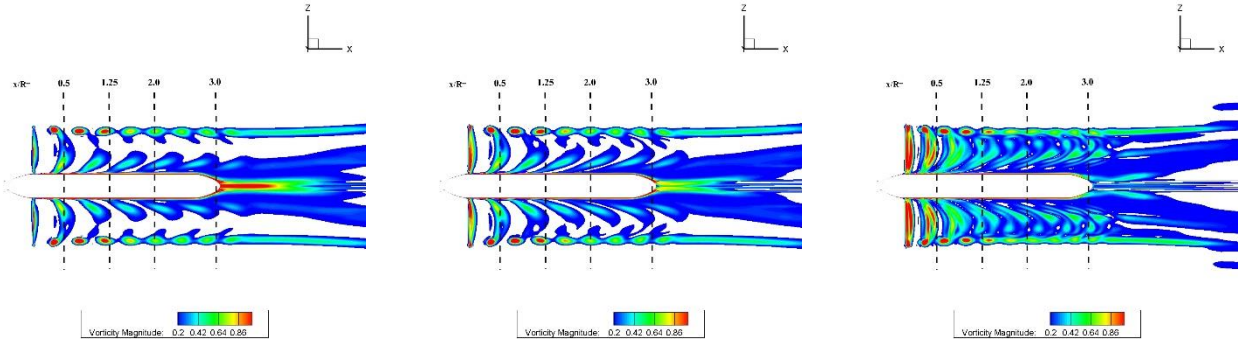
## 5.3 Influence of DT

This section analyzes the effect of DT while keeping other simulation parameters constant. CFLTAU is set to 1.0, NCYC is set to 10, and DT takes values of 0.02, 0.04, and 0.08, respectively.

Figure 14 presents the iso-surface contours of the propeller wake vorticity and the vorticity contours on the axial cross-section under different DT settings. It can be observed from Figure 14 that, with other parameters unchanged, as DT increases, the rotation angle of the dynamic blade loads between consecutive time steps becomes excessively large. This increases the difficulty of convergence in the pseudo-time iterations, leading to gradual distortion of the vortex structure and reduced vortex resolution. At the same time, the adhesion phenomenon between the blade root vortex and the blade tip vortex becomes increasingly evident with larger DT, and the degree of trailing vortex dissipation increases accordingly.




(a) iso-surface contours of DT=0.02 (b) iso-surface contours of DT=0.04 (c) iso-surface contours of DT=0.08




(d) vorticity contours of DT=0.02 (e) vorticity contours of DT=0.04 (f) vorticity contours of DT=0.08

Figure 14 The Influence of Different DT Settings on the Propeller Slipstream

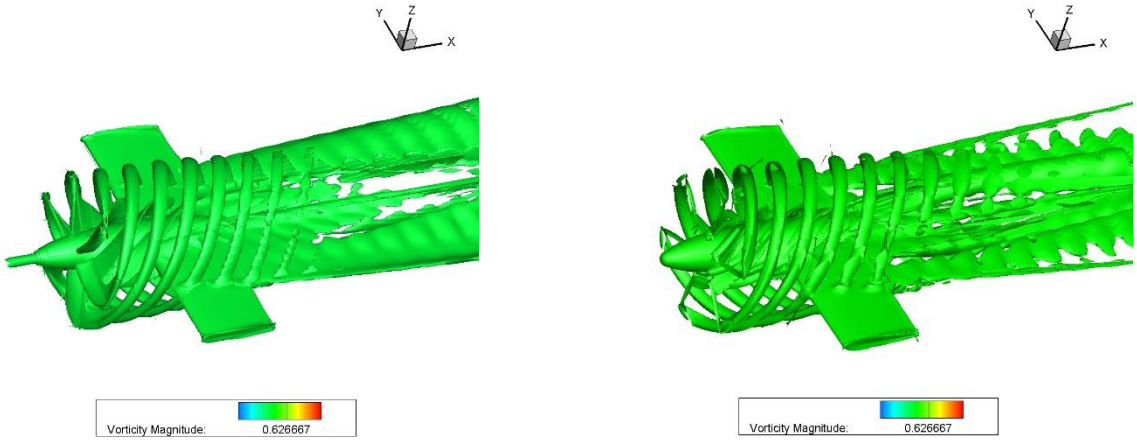
## 6. Comparison of Simulation Results for the Propeller-Wing Configuration

Since the full mesh rotation method cannot be applied to configurations with propellers, this section performs numerical simulations of the propeller-wing configuration using two methods: the FBM and the ABM. The load file used in the actuator blade method is extracted from the propeller loads simulated for the propeller-wing configuration.

For the propeller-wing configuration, the propeller center is located at x=0, the dynamic sliding interface is located at x=0.8, the wing leading edge is at x=1.981, and the wing trailing edge is at x=3.946. For the disk-propeller configuration, the disk center is also at x=0, with all other geometric positions consistent with the propeller-wing configuration. Comparative calculations are performed under two operating conditions, with the angle of attack set to $0^{\circ}$ and $2^{\circ}$ respectively, while all other physical parameters remain unchanged.

### 6.1 Comparison of Simulation Results At $\alpha = 0$

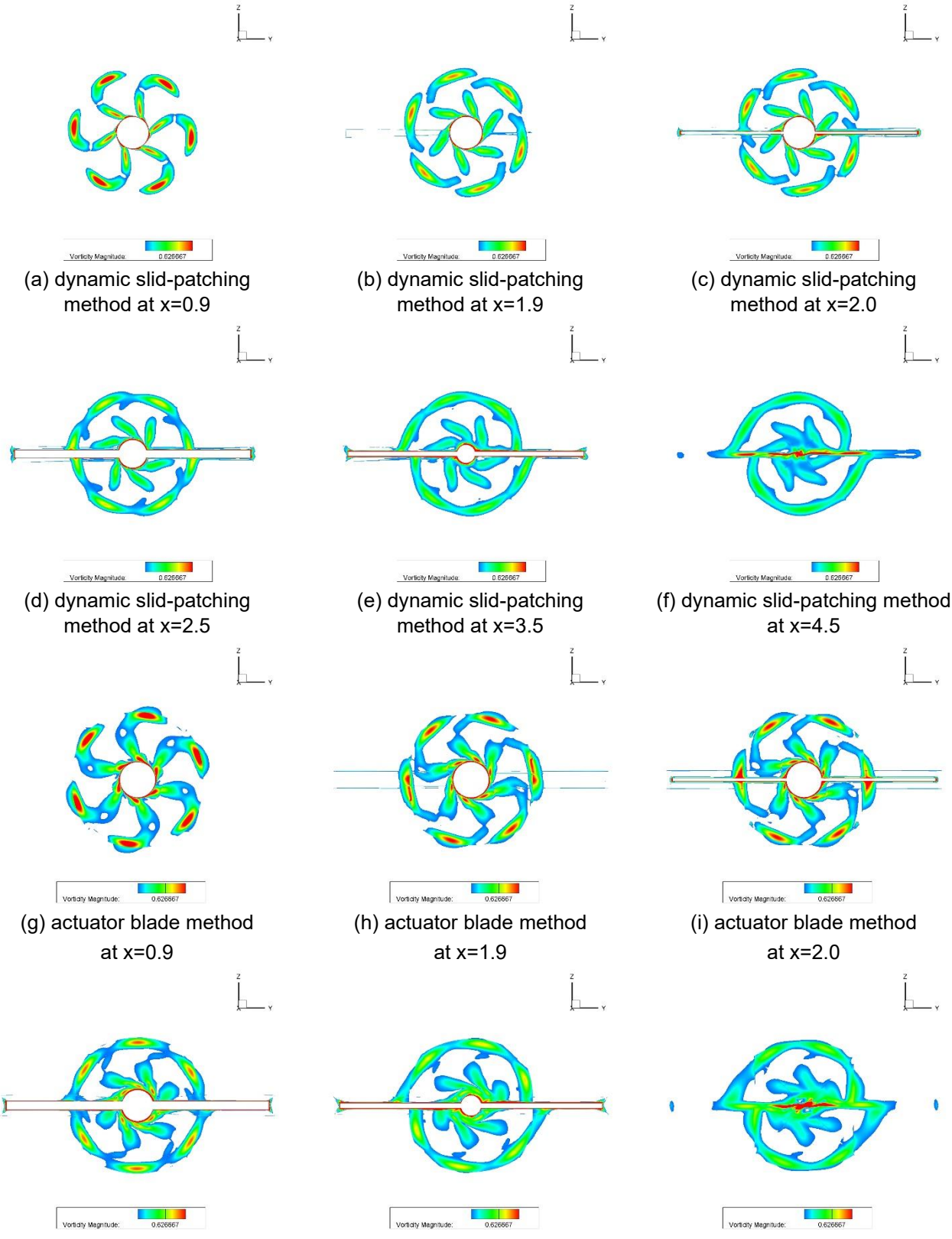
Figure 15 presents the iso-surface contours of the propeller slipstream using two different simulation methods. Simulating by the two methods, Figure 16 compares the vorticity contours of the propeller slipstream at the same axial stations, Figure 17 shows the comparison curves of the aerodynamic coefficients of the wing and Figure 18 compares the pressure distributions at different spanwise stations on the wing surface.




(a) dynamic slid-patching method (b) actuator blade method

Figure 15 Iso-surface Contours of the Propeller Slipstream using Two Methods

From Figure 15, it can be seen that employing the same simulation parameters, the vorticity iso-surface contours of the propeller obtained by the ABM show good agreement with those obtained by the FBM.




(a) dynamic slid-patching method at x=0.9 (b) dynamic slid-patching method at x=1.9 (c) dynamic slid-patching method at x=2.0

(d) dynamic slid-patching method at x=2.5 (e) dynamic slid-patching method at x=3.5 (f) dynamic slid-patching method at x=4.5

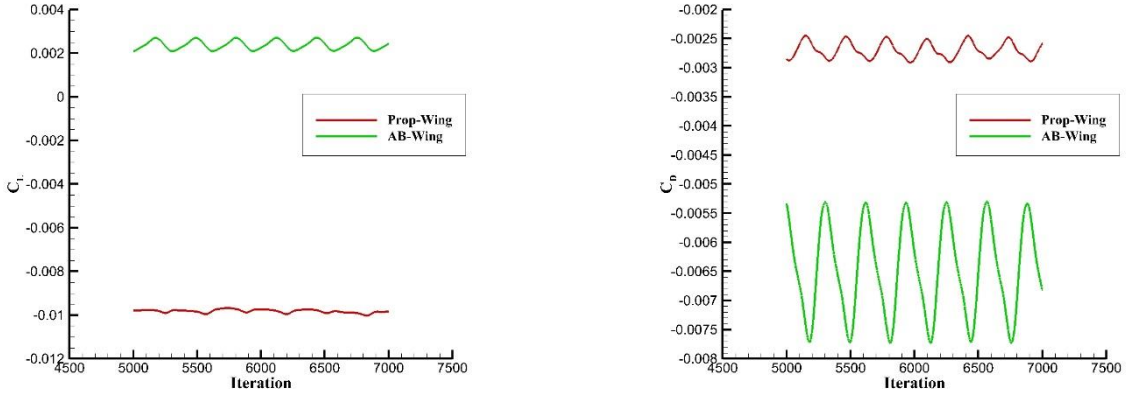
(g) actuator blade method at x=0.9 (h) actuator blade method at x=1.9 (i) actuator blade method at x=2.0

(j) actuator blade method at x=2.5 (k) actuator blade method at x=3.5 (l) actuator blade method at x=4.5

Figure 16 Vorticity Contours of the Propeller Slipstream Using Two Methods

From Figure 16, the vorticity contours at each cross-section obtained by the two methods are in high agreement. However, at every cross-section, the vorticity intensity obtained by the ABM is higher

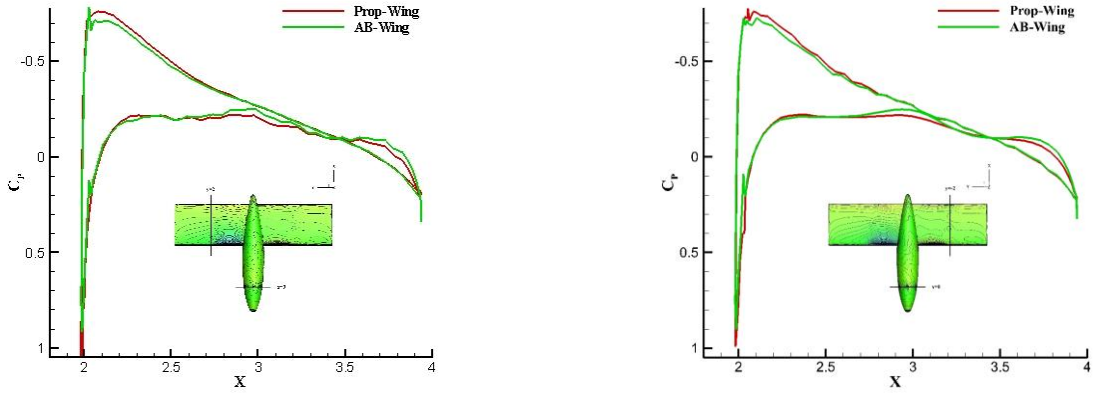
than that from the FBM. Especially at the x=2.5 and x=3.5 cross-sections, the slice contours from the FBM fail to display clear blade tip vortices, while the results from the ABM still show distinct tip vortex positions with substantial vorticity intensity. This indicates that under the same conditions, the losses experienced by the propeller slipstream when passing through the dynamic sliding interface in the FBM affect the subsequent development of the vorticity and the interaction with the wing.



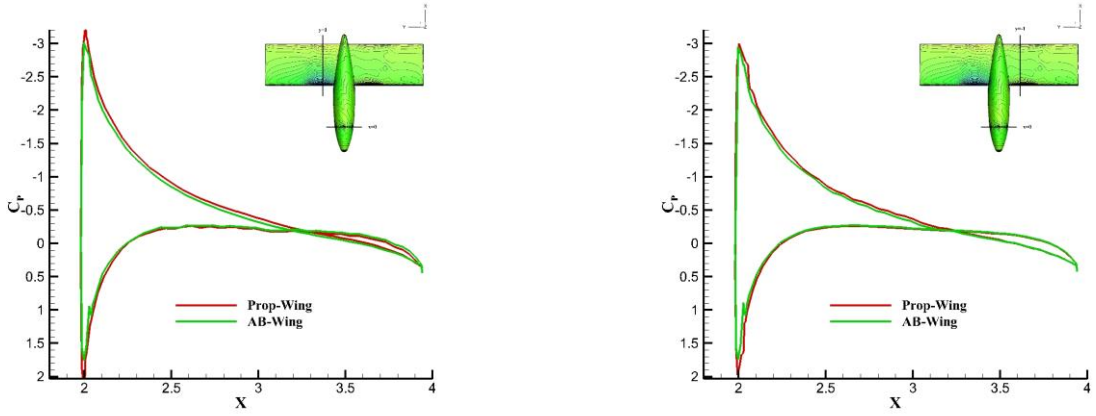

(a) comparison curves of $C_L$-Iteration (b) comparison curves of $C_D$-Iteration

Figure 17 Comparison Curves of the Aerodynamic Coefficients of the Wing Using Two Methods

From Figure 17, it can be seen that within approximately one revolution period, the wing lift and drag coefficient curves obtained by both methods oscillate six times, which is consistent with the unsteady fluctuation pattern of a six-bladed propeller. From the lift coefficient comparison curve, since the angle of attack is $0^\circ$, the lift coefficients are both small in magnitude. The lift coefficient curve obtained by the FBM shows weak oscillation, while the curve from the ABM exhibits clear and large-amplitude oscillation. From the drag coefficient comparison, since the propeller slipstream region occupies 53% of the wing span, the simulated wing drag appears as negative drag, i. e., thrust. The peak value and oscillation amplitude of the drag coefficient curve from the FBM are both smaller than those from the ABM. These results indicate that the slipstream influence on the wing simulated by the ABM is more pronounced than that obtained by the FBM.




(a) Y=2_alpha=0 (b) Y=-2_alpha=0



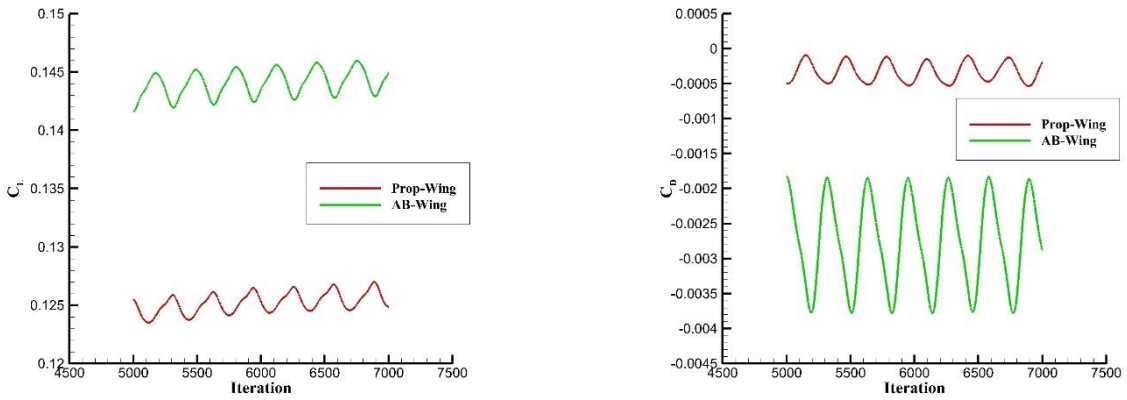

(c) Y=1_alpha=0 (d) Y=-1_alpha=0

Figure 18 Pressure Distributions at Different Spanwise Stations on the Wing Surface

During the simulation, the initial rotation phase of the blades in the FBM differs from that of the ABM. Due to the unsteady periodic characteristic of the propeller slipstream, the wing surface pressure distributions simulated by the two methods exhibit a certain phase difference at the same instant. To more intuitively demonstrate the magnitude of the unsteady phenomena on the wing surface obtained by the two methods, the pressure distribution curves are processed to align them at the same phase. From Figure 18, it can be observed that within the slipstream region(at the Y=1 and Y=-1 cross-section), the suction peak of the pressure distribution curve simulated by the ABM is slightly lower than that obtained by the FBM. The overall trend and shape of the curves show an extremely high degree of agreement, indicating good consistency between the two methods within the slipstream region. At the edge of the slipstream region(at the Y=2 and Y=-2 cross-section), It can be seen that the curves from two methods are consistent in their development trend and shape. The fluctuation amplitude of the pressure distribution within the high-pressure region of the wing simulated by the ABM is slightly higher than that predicted by the FBM. This indicates that the vortex intensity simulated by the ABM and the unsteady influence of the propeller slipstream on the wing are greater than that obtained by the FBM.

## 6.2 Comparison of Simulation Results At $\alpha = 2^0$

This section presents a comparison of the results obtained by the two methods at an angle of attack of $2^\circ$, to give a clear slipstream influence on lift of the wing, and shown in Figure 19.




(a) comparison curves of $C_L$-Iteration (b) comparison curves of $C_D$-Iteration

Figure 19 Comparison Curves of the Aerodynamic Coefficients of the Wing Using Two Methods

From the lift coefficient comparison, under the same simulation conditions, the peak lift coefficient

obtained by the ABM is approximately 0.145, while that from the FBM is approximately 0.126. The ABM increases the lift coefficient by about 0.019, corresponding to an increase of approximately 15%. Additionally, the oscillation amplitude of the lift coefficient from the ABM is slightly larger than that from the FBM.

From the drag coefficient comparison, under the same simulation conditions, the drag coefficient generated by the swirling slipstream on the wing using the ABM is greater than that simulated by the FBM. The peak of drag coefficient obtained by the FBM is approximately -0.0005, while the result obtained by the ABM is approximately -0.0037. The oscillation amplitude of the drag coefficient from the ABM is also larger than that from the FBM. Based on the above analysis, it can be concluded that the propeller slipstream obtained by the ABM is stronger in intensity, and the unsteady influence on the wing is more pronounced.

## 7. Conclusion

This paper uses the CFL3D solver, employing its sliding mesh module to perform calculations with dynamic slid-patching method. Based on the original CFL3D solver, actuator blade module was developed. Through numerical simulations of the isolated propeller configuration and the propeller-wing configuration, the simulation accuracy of the propeller slipstream is analyzed and compared for three methods: the full mesh rotation method, the dynamic slid-patching method, and the actuator blade method. Based on the above calculations and analyses, here gives following conclusions:

1) Numerical simulation with full mesh rotation method expects high accuracy for the isolated rotating propeller, but it cannot be used for the situation which has relative motion between propeller and other aircraft components. The dynamic slid-patching method has the broadest applicability and can be used for nearly all propeller-equipped configurations. Nevertheless, due to significant numerical dissipation across the dynamic patched interface, the impact of the slip stream will be weakened. Similar to the full mesh rotation method, the actuator blade method needn't to deal with the patched interface. Furthermore, the actuator blade method requires less simulation cost and has a wider range of applications compared to the full mesh rotation method. It is therefore a more efficient and reliable numerical method for propeller slipstream simulation.

2) For the isolated actuator blade propeller configuration, a systematic survey is adopted to analyze the effects of three key simulation parameters. With the increase in NCYC, the increase in CFLTAU, and the decrease in DT, the morphology of the propeller slipstream vortex becomes gradually clearer. The adhesion between the blade tip vortex and blade root vortex is weakened, vortex dissipation is reduced, and the accuracy and resolution of the numerical simulation are improved.

3) For the propeller-wing configuration, the vortex intensity obtained by the ABM is greater than that simulated by the FBM. Consequently, the unsteady oscillation amplitudes of the wing lift and drag coefficients and wing surface pressure distribution curves computed by the ABM are larger than those from the FBM. Above all, ABM is an efficient numerical simulation method for propeller slipstream.

## 8. Contact Author Email Address

Jiawen He:18291773787@163.com

## 9. Copyright Statement

The authors confirm that they, and/or their company or organization, hold copyright on all of the original material included in this paper. The authors also confirm that they have obtained permission, from the copyright holder of any third party material included in this paper, to publish it as part of their paper. The authors confirm that they give permission, or have obtained permission from the copyright holder of this paper, for the publication and distribution of this paper as part of the ICAS proceedings or as individual off-prints from the proceedings.

## References


[1] Xia Z F., “Numerical Approaches of Propeller Slipstream Simulation and Aerodynamic Interference Analysis”. Doctorate Degree, Xi’an: Northwestern Polytechnical University, 2015.

[2] Muller, Lars, Heinze, Wolfgang, Kozulovic, Dragan, et. Al. Aerodynamic Installation Effects of an Over-the-Wing Propeller on a High-Lift Configuration[J]. *Journal of Aircraft*, 2014,51,(1):249-258.

[3] Beyers Martin, “ Unsteady wind-tunnel interference in dynamic testing”, *29th Aerospace Sciences Meeting*, Reno, Nevada, 1991.

[4] Le Chuiton Frédéric, " Actuator disc modelling for helicopter rotors", *Aerospace Science and Technology* (2004) 8, 285-297.

[5] Wales Christopher, Jones Dorian, Gaitonde Ann, et al, " Comparison of Aircraft Loads Using URANS and Actuator Disk Modelling of Propellers", *AIAA AVIATION* 2022 Forum, Chicago, 2022.

[6] Yang Longyuan, Sheng Yunyi, Yang Yong, " Numerical Simulation of propeller slip-stream influence on the high lift configuration with Actuator Disk Method", *12th International Conference on Computational Fluid Dynamics*, Kobe, Japan, 2024.

[7] Fejtek Ian, Roberts Leonard, " Navier-Stokes Computation of Wing/Rotor Interaction for a Tilt Rotor in Hover", *AIAA Journal* (1992) Volume 30, P2585-P2808.

[8] Rajagopalan R. Ganesh, Mathur Sanjay R., " Three dimensional analysis of a rotor in forward flight", *20th Fluid Dynamics*, Plasma Dynamics and Lasers Conference, Buffalo, NY,U.S.A., 1989.

[9] Sørensen J. N., Shen W. Z., " Numerical Modeling of Wind Turbine Wakes", *Journal of Fluids Engineering* (2002) No. 2, 393-399.

[10] Linton Daniel, Widjaja Ronny, Thornber Ben, " Actuator Surface Model with Computational-Fluid-Dynamics-Convected Wake Model for Rotorcraft Applications", *AIAA Journal* (2021).

[11] Kim Y. H., Park S. O., " Unsteady Momentum Source Method for Efficient Simulation of Rotor Aerodynamics", *Journal of Aircraft* (2013) Vol. 50.

[12] Kulfan Brenda, " Recent Extensions and Applications of the “ CST ” Universal Parametric Geometry Representation Method", *7th AIAA Aviation Technology*, Integration and Operations Conference, Belfast, Northern Ireland, 2007.